Volume 1 | Number 1 | Jan 2013 | Pages 1–100

Journal of
**Materials Chemistry C**

Materials for optical and electronic devices
www.rsc.org/materialsC

ROYAL SOCIETY
OF CHEMISTRY

ROYAL SOCIETY
OF **CHEMISTRY**

www.rsc.org/materialsC

# Journal of Materials Chemistry C

Dynamic Article Links ▶

**Full Papers**

# Precise Adjustment of Structural Anisotropy and Crystallinity on Metal-Fe₃O₄ Hybrid Nanoparticles and Its Influence on Magnetic and Catalytic Properties

**Mijong Kim and Hyunjoon Song***

In the present study, we demonstrate the precise adjustment of morphology and crystallinity of metal (Pd or Au)-Fe₃O₄ hybrid nanoparticles by reaction kinetics control. The nucleation and growth of the Fe component on the Pd surface are precisely controlled by using a mixture of capping agents, oleylamine ₁₀ and oleic acid. After the oxidation, the resulting Pd-Fe₃O₄ structures are produced as yolk-shell, irregular core-shell, and dumbbell-like NPs. Along with the morphology change, the average crystal domain size of Fe₃O₄ and the void gap between the metal cores and the shells are simultaneously adjusted. The crystal domain sizes of Fe₃O₄ directly influence the magnetic property, and the structural arrangement of the Pd cores and the Fe₃O₄ shells leads to a large difference of conversion yields in the Suzuki coupling ₁₅ reactions. Our approach is successfully extended to other metal-Fe₃O₄ hybrid systems, such as those of Au and Fe₃O₄.

## 1. Introduction

For the past decade, hybrid nanoparticles (NPs) have been an important research area in the field of nanoscale materials owing ₂₀ to their multi-functional properties.[1-3] In particular, a variety of metal oxides have been combined with metals to form metal-metal oxide hybrid NPs for the sake of high stability of oxides and for potential catalytic applications. Among these oxides, a magnetite, Fe₃O₄, has been intensively pursued as a stable ₂₅ magnetic component.[4,5] Nanostructures containing metals and Fe₃O₄ have been employed as recyclable model catalysts for organic reactions.[6-10] The dumbbell-like Au-Fe₃O₄ NPs were used as a catalyst for CO oxidation to CO₂, and as a platform for multimodal imaging and therapeutics.[11-13] The PtPd-Fe₃O₄ NPs ₃₀ showed enhanced catalytic activity for H₂O₂ reduction reaction.[14] Apparently, the size, shape, and crystallinity of each domain and the interfaces between distinct domains are critical factors that dominate the physico-chemical properties of hybrid NPs. Although several shapes have been synthesized,[15-17] the relations ₃₅ between final morphology, crystallinity, and accompanied properties need to be rationally explored in hybrid NP systems. Schevchenko et al. reported that the thickness of Fe₃O₄ shells was controlled by the variable ratio of oleylamine/oleic acid in the Au@Fe₃O₄ core-shell nanoparticles.[15] Recently, George et al. ₄₀ successfully converted the Au@Fe₃O₄ core-shell nanoparticles into heterodimers by annealing at high temperature, and dissolved the Au particles for the synthesis of Fe₃O₄ concave nanoparticles.[18]

In the present study, we chose a hybrid system comprising Pd ₄₅ and Fe₃O₄ components. The nucleation and growth of the Fe component on the Pd surface were precisely controlled by using a mixture of capping agents, oleylamine (OAm) and oleic acid (OA). After the oxidation, the resulting Pd-Fe₃O₄ structures were produced as yolk-shell (**Pd-1**), irregular core-shell (**Pd-2**), and ₅₀ dumbbell-like (**Pd-3**) NPs. Along with the morphology change, the average crystal domain size of Fe₃O₄ and the exposed surface area of Pd outward were simultaneously altered, which directly affected the magnetic and catalytic properties, respectively. Our approach was successfully extended to other metal-Fe₃O₄ hybrid ₅₅ systems, such as those of Au and Fe₃O₄.

## 2. Experimental Section

**Chemicals:** Palladium(II) acetylacetonate (Pd(acac)₂, 99%), oleylamine (OAm, 70%), trioctylphosphine (TOP, 90%), iron(0) pentacarbonyl (99.999%), oleic acid (OA, 90%), 1-octadecene ₆₀ (90%) were purchased from Aldrich. Hexane (99.5%) was purchased from Junsei. The chemicals were used as received without further purification and treated under an inert atmosphere.

**Synthesis of Pd Seeds:** A mixture of Pd(acac)₂ (91 mg, 0.30 ₆₅ mmol), trioctylphosphine (1.0 mL, 2.3 mmol), and OAm (10 mL) was heated to 503 K for 20 min under a nitrogen atmosphere, and was allowed to stir for additional 40 min. The reaction mixture was cooled down to room temperature, and the Pd nanoparticles were collected by centrifugation in ethanol. The black precipitate ₇₀ was re-dispersed in 1-octadecene.

**Formation of Pd-Fe₃O₄ hybrid NPs:** All reactions were carried out under the inert atmosphere. Iron(0) pentacarbonyl (Fe(CO)₅, 0.10 mL, 0.76 mmol), OAm, OA, and the Pd seed dispersion (0.15 mmol with respect to the Pd content) were injected into 1-octadecene (total 20 mL) at room temperature. The reaction mixture was heated to 573 K for 15 min, and allowed to stir at 573 K for 45 min. After cooling the mixture in air, the product was precipitated by adding ethanol (30 mL) and thoroughly washed by a repetitive dispersion (by sonication) – precipitation (by centrifugation) cycle with hexane (15 mL) and ethanol (90 mL).

For **Pd-1**, OAm (2.0 mL, 6.1 mmol) was used as the only capping agent. For **Pd-1'**, a mixture of OA (0.2 mL, 0.6 mmol) and OAm (1.8 mL, 5.5 mmol), for **Pd-2**, a mixture of OA (0.5 mL, 1.6 mmol) and OAm (1.5 mL, 4.6 mmol), and for **Pd-3**, a mixture of OA (1.0 mL, 3.2 mmol) and OAm (1.0 mL, 3.0 mmol) were used for the reaction, respectively.

**Suzuki Coupling Reactions:** Iodobenzene (0.11 mL, 1.0 mmol, 1.0 equiv), phenylboronic acid (1.5 g, 1.2 mmol, 1.2 equiv) and K₂CO₃ (0.41 g, 3.0 mmol, 3.0 equiv) were added to the solvent mixture (THF : water = 8 : 3) in the presence of catalysts, **Pd-1** or **Pd-3** (1.5 mol% with respect to the Pd content), in a stainless steel autoclave. The mixture was vigorously stirred at 373 K for either 36 h or 12 h. After cooling the reaction mixture, the catalysts were separated by a magnetic force. The product mixture was extracted with ethyl acetate (EA) and brine. Drying with MgSO₄, filtration, and solvent evaporation of the filtrate yielded the reaction products. The conversion yields were determined by ¹H NMR. For the recycling experiments, after the reaction, the catalyst particles were separated by a magnetic force, and washed with EA. The particles were redispersed in THF (8.0 mL), and were used as catalysts for another cycle of the reaction.

**Synthesis of Au Seeds:** A mixture of AuCl₃ (91 mg, 0.30 mmol) and OAm (10 mL) was heated to 230 °C for 15 min under a nitrogen atmosphere, and was additionally stirred for 45 min at the same temperature. The reaction mixture was cooled down to room temperature, and the Au nanoparticles were precipitated by centrifugation in ethanol. The dark red product was redispersed in hexane.

**Formation of Au-Fe₃O₄ hybrid NPs:** The procedures are identical to those of Pd-Fe₃O₄ hybrid NPs, except the Au seed dispersion in hexane (3.0 mL, 0.15 mmol with respect to the Au content), Fe(CO)₅ (0.020 mL, 0.15 mmol), and capping agents. For **Au-1**, OAm (2.0 mL, 6.1 mmol) was used as the only capping agent. For **Au-1'**, a mixture of OA (0.2 mL, 0.6 mmol) and OAm (1.8 mL, 5.5 mmol), for **Au-2**, a mixture of OA (0.3 mL, 0.1 mmol) and OAm (1.7 mL, 5.2 mmol), and for **Au-3**, a mixture of OA (0.4 mL, 1.3 mmol) and OAm (1.6 mL, 4.9 mmol) were used for the reaction, respectively.

**Characterization:** The catalyst particles were characterized by transmission electron microscopy (Philips F20 and F30 Tecnai operated at 200 and 300 kV, KAIST; JEOL JEM-ARM200F, NNFC; EF-TEM AE12, KBSI). The particle dispersion was drop-casted on carbon-supported 300 mesh and ultrathin 400 mesh Cu grids (TED PELLAR, INC). The X-ray diffraction (XRD) patterns and X-ray photoelectron spectral data were recorded on a Rigaku D/MAX-2500 (18 kW) diffractometer and Sigma Probe

(XPS (UPS), Thermo VG Scientific), respectively. The magnetic properties were measured using a superconducting quantum interference device (SQUID) magnetometer (MPMS5). The Pd content of each sample was determined by an inductively coupled plasma-atomic emission spectrometer (ICP-AES, POLY SCAN 60 E). The C-C coupling reaction products were analyzed by ¹H NMR using BRUKER AVANCE 300 MHz.
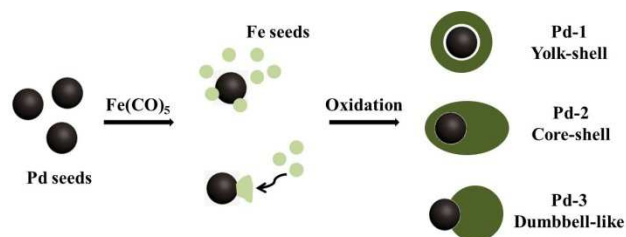


**Scheme 1** Schematic illustration of the synthesis of Pd-Fe₃O₄ hybrid NPs.

## 3. Results and Discussion

### 3.1. Synthesis of Pd-Fe₃O₄ hybrid nanoparticles

Spherical Pd NPs with an average diameter of 4.2±0.4 nm were synthesized according to the literature,[19-21] and these materials were used as seeds. The Fe precursor, Fe(CO)₅, was thermally decomposed on the surface of the Pd NPs in the presence of surfactants, OAm and OA, with a variable ratio, followed by further growth and air-oxidation (Scheme 1). Without the Pd NPs, the present reaction conditions yielded Fe₃O₄ hollow and irregular NPs (Supporting Information, Figure S1). When OAm was the only capping agent (Fe(CO)₅ : OAm : OA = 1 : 8 : 0), the reaction mixture immediately changed its color to dark brown, indicating the rapid decomposition of the Fe precursor (Supporting Information, Figure S2). The transmission electron microscopy (TEM) image of the resulting particles (**Pd-1**) shows a concentric Pd@Fe₃O₄ yolk-shell morphology with high uniformity (Figure 1a).[22,23] In the high magnification HAADF-STEM (high angle annular dark field-scanning transmission electron microscopy) image, a void between the Pd core and Fe₃O₄ shell is clearly seen and EDX (energy dispersive X-ray spectroscopy) line-scanning across a single Pd@Fe₃O₄ NP reveals that Pd is confined at the center position while Fe and O are distributed over all cross section of the NP. (Figure S3a and b) As in a typical yolk-shell type structure, the Pd cores in **Pd-1** are clearly isolated from the Fe₃O₄ shells through voids, without direct contact. The average diameter of **Pd-1** is estimated to be 8.3±0.5 nm, and the average thickness of the Fe₃O₄ shells is 2.6±0.2 nm. The high resolution TEM (HRTEM) image of an individual **Pd-1** reveals that both the Pd core and the Fe₃O₄ shell are polycrystalline; the average distances of the adjacent lattice fringe images were measured to be 0.225 and 0.254 nm, which values correspond to the interplanar spacing of (111) planes of face-centered cubic Pd and (311) planes of magnetite Fe₃O₄, respectively (Figure 1b).

With the addition of OA to the reaction mixture, the reaction speed was significantly retarded. In the condition of a small amount of OA (Fe(CO)₅ : OAm : OA = 1 : 7.2 : 0.8), the final morphology of the product (**Pd-1'**) began to lose its high symmetry. Figure 1c and d show that the Fe₃O₄ shells are
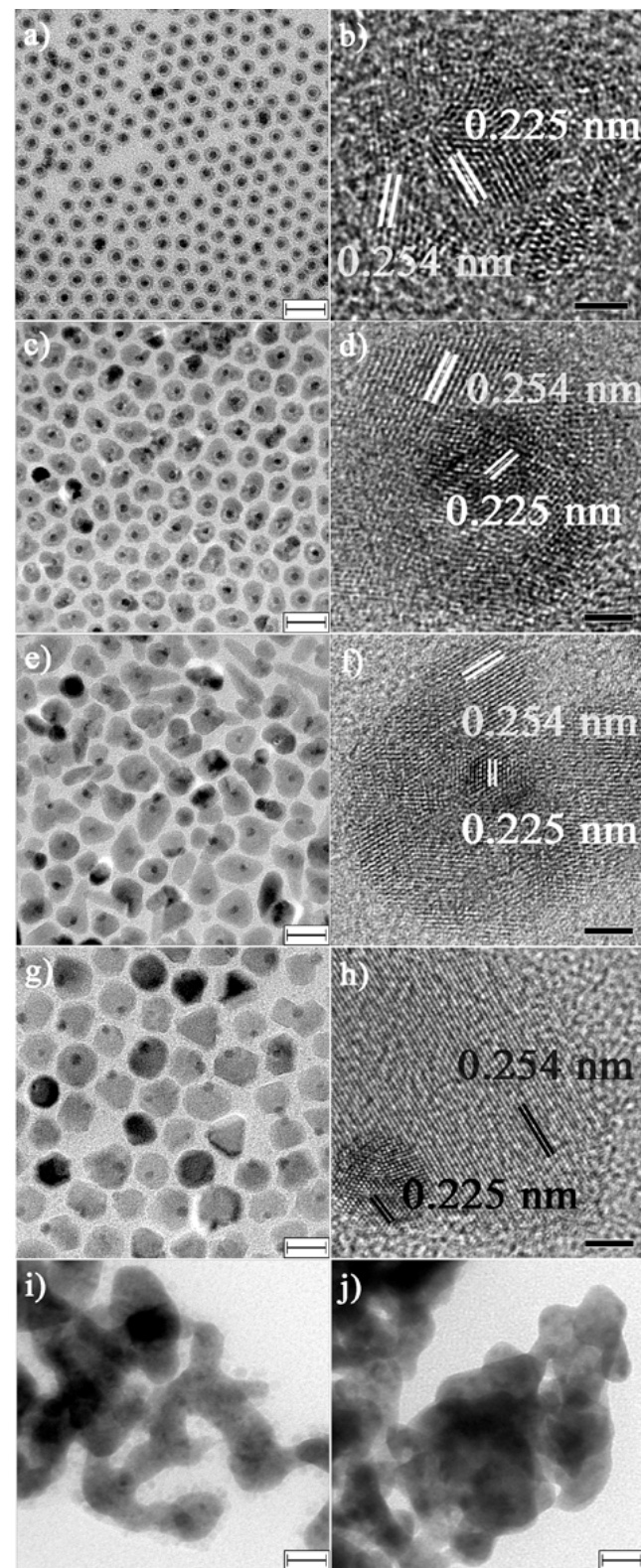
**Fig. 1** TEM and HRTEM images of Pd-Fe$_3$O$_4$ hybrid NPs; (a, b) **Pd-1**; (c,
d) **Pd-1'**; (e, f) **Pd-2**; and (g, h) **Pd-3**; (i, h) TEM images of Pd-Fe clumps
formed under molar ratios of Fe(CO)$_5$:OAm:OA; 1 : 2 : 6.2 and 1 : 0 : 8.3.
The scale bars represent (a, c, e, g, i, j) 20 nm and (b, d, f, h) 2 nm.
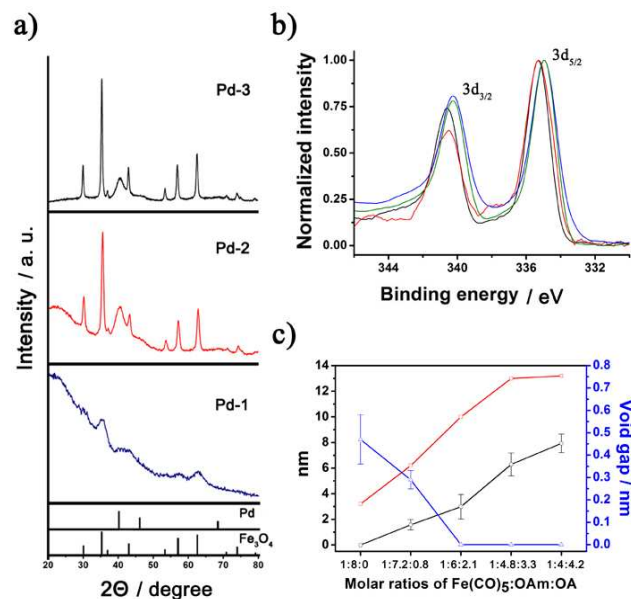


**Fig. 2** (a) XRD data of **Pd-1**, **Pd-2**, and **Pd-3**. (b) XPS data of
freestanding Pd NPs (green), **Pd-1** (blue), **Pd-2** (red), and **Pd-3** (black) in
the Pd 3d level. (c) The relationship of the ratio of capping agents versus
average acentric distance (black), crystal domain size (red), and void gap
(blue) of each nanostructure. The acentric distance is defined as the
distance between the Pd core and the center of symmetry.

asymmetrically formed around the Pd cores, and thus the Pd
cores are slightly off from the center of symmetry. The shell is
not uniformly round, but the void between the core and the shell
still exists in each structure. As the molar ratios of OA and OAm
increased (Fe(CO)$_5$ : OAm : OA = 1 : 6 : 2.1), the time of the
color change of the reaction mixture slowed to 20 min
(Supporting Information, Figure S2). The resulting particles (**Pd-
2**) have a Pd@Fe$_3$O$_4$ core-shell structure without any voids
(Figure 1e). The Fe$_3$O$_4$ shells are composed of a few distinctive
domains; each domain is single-crystalline with a size of ~10 nm
(Figure 1f). Additional increase of the molar ratio of OA and
OAm (Fe(CO)$_5$ : OAm : OA = 1 : 4 : 4.2) generated a dumbbell-
like morphology of Pd-Fe$_3$O$_4$ (**Pd-3**, Figure 1g). Figure 1h clearly
shows that the Pd domain is eccentrically attached on one side of
the Fe$_3$O$_4$ polyhedron. The Fe$_3$O$_4$ domains are single-crystalline,
and an average size of the domains, from the junctions of Pd-
Fe$_3$O$_4$ to the end of the Fe$_3$O$_4$ edges, is estimated to be 14 ± 2 nm.
The **Pd-3** is stable without detachment of the Pd domains during
prolonged sonication. When the OA was the only capping agent,
the product was large metal clumps without crystal formation
(Figure 1i and j).

## 3.2. Structural parameters of hybrid nanoparticles

The X-ray diffraction (XRD) data for **Pd-1**, **Pd-2**, and **Pd-3**
(Figure 2a) are composed of face-centered cubic Pd (JCPDS No.
46-1043) and inverse spinel Fe$_3$O$_4$ (JCPDS No. 01-1111) patterns,
according to the literatures.[16,24] However, for iron oxides, Chaboy

et al. have recently characterized magnetite NPs by using X-ray absorption near edge spectroscopy, and precisely analyzed that the actual components of the magnetite NPs were actually a non-stoichiometric $Fe_{3-\delta}O_4$ with the cation vacancies, irrespective of the synthesis method.[25] The diffraction patterns of Pd are broad due to the small size of the Pd domains. On the other hand, the patterns originating from the $Fe_3O_4$ component are largely sharpened from **Pd-1** to **Pd-3**, as directly shown in the HRTEM images. The single-crystal domain sizes, estimated using the Scherrer formula, are 3.2, 10.0, and 13.2 nm for **Pd-1**, **Pd-2**, and **Pd-3**, respectively. X-ray photoelectron spectroscopy (XPS) measurement was conducted for the quantitative measurement of the electronic interaction between the Pd and $Fe_3O_4$ domains (Figure 2b). The electron binding energy of the Pd 3d level was measured with the C 1s level setting to 284.5 eV as a reference. The freestanding Pd NPs and **Pd-1** have peaks at 335 eV for $3d_{5/2}$, whereas **Pd-2** and **Pd-3** show significant shifts of 0.3 eV toward the higher binding energy. These data demonstrate that the Pd cores in **Pd-1** are not in electronic contact with the $Fe_3O_4$ shells due to the void, but in **Pd-2** and **Pd-3**, a significant fraction of the Pd domains contacts with the $Fe_3O_4$ domains, and leads to electron transfer from Pd to $Fe_3O_4$, resulting in the high energy shifts of the XRD peak. Such electron transfer reflects the work function difference of Pd (5.22 eV)[26] and $Fe_3O_4$ (5.52 eV).[27]

Figure 2c shows the relationship between the ratio of the capping agents used in the synthesis and the structural parameters of the final products. From **Pd-1** to **Pd-3**, the usage of OA with respect to that of OAm increased, and the reaction rate diminished (Supporting Information, Figure S2). In order to demonstrate the structural symmetry change by the ratio of capping agents, the acentric distance was defined as the distance between the center of the Pd core and the center of the total structure. The average acentric distance (black) linearly increased from **Pd-1** to **Pd-3**, indicating that symmetry alteration occurred due to the increase of OA concentration. The average crystal domain size (red) of the $Fe_3O_4$ component, determined from the XRD signals, also increased from polycrystalline **Pd-1** to single-crystalline **Pd-3**. On the contrary, the average void gap between the Pd cores and the $Fe_3O_4$ shells (blue) diminished from **Pd-1** to **Pd-2** to form core-shell NPs without voids. Briefly, the increment of the OA concentration during the synthesis increased the structural anisotropy and the crystal domain size of $Fe_3O_4$, but decreased the void gap between the Pd and $Fe_3O_4$ domains.

### 3.3. Formation mechanism and morphology change

$Pd$-$Fe_3O_4$ NPs were prepared via a two-step process. First, the Fe precursor was decomposed to generate Fe atomic seeds, and Fe domains were grown on the Pd surface by the Ostwald ripening process.[28] Then, slow air oxidation eventually yielded the $Fe_3O_4$ phase. During the nucleation and growth, the presence of OA was critical to adjust the reaction rate. OAm behaved as a stabilizing agent;[29] however, OA was strongly bound to Fe and oxidized into +1 or +2 valence states, forming an Fe-oleate complex with a high nucleation barrier.[30] Consequently, the increase of the OA concentration reduced the number of Fe atomic seeds and retarded the growth rate. A small number of the seed surface in the reaction mixture and low supersaturation due to slow

decomposition of the Fe-oleate complex led to the formation of large crystals,[31,32] and thus the crystal domain size increased with the addition of OA. Such a reaction mechanism simultaneously influenced the structural anisotropy of the final morphology. During the nucleation process, a large number of Fe atomic seeds were formed and covered the entire Pd surface, when OAm was the only capping agent. The fast growth on the seeds yielded a totally symmetrical structure of **Pd-1** with tiny single-crystal domains. In **Pd-3**, an extremely small number of the seeds were attached on the Pd surface, and slow growth formed large single-crystal Fe domains with the original Pd seeds attached at one side. The adjustment of the ratio of OA and OAm in-between precisely changed both the structure and the crystal domain size from **Pd-1** to **Pd-3**.

During the air oxidation process, void gaps were generated through the nanoscale Kirkendall effect.[33] Oxygen diffused into the confined structure mainly through vacancies such as grain boundaries and unstable defects, and reacted with Fe to form $Fe_3O_4$. By considering the steady state diffusion and Fick's first law, the time required to fill the void can be estimated to be:

$$t = \left( \frac{kT}{A\gamma D\Omega} \right) r^3 \tag{1}$$

where A is a constant, $\gamma$ is the surface energy per unit area, $D$ is the self-diffusion coefficient, $\Omega$ is the atomic volume of the vacancies, and $r$ is the inner radius in a spherical hollow NP.[34] For the formation of hollow particles at the synthesis temperature, the formation time must be shorter than $t$. This equation indicates that the minimum vacancy volume ($\Omega$) is inversely proportional to the reaction time ($t$). In the model of binary diffusion in a continuous and dense vacancy source, the elapsed time $t'$, required to reach the final equilibrium state in the diffusion couple decreases as the number of grain boundaries increases.[35] Therefore, the inverse relationship of the crystal domain size and the void gap shown in Figure 2c could be explained as follows: in **Pd-1**, the Fe shells had small single-crystal domains with dense grain boundaries, and thus the resulting short elapsed time of diffusion generated large voids between the Pd cores and the $Fe_3O_4$ shells. On the contrary, the large single-crystal domains in **Pd-2** had an elapsed time for oxidation longer than $t$, leading to no void formation inside the $Fe_3O_4$ shells.

### 3.4. Crystallinity and magnetic properties

The high tunability of the single-crystal domain size of the iron oxide components directly influenced their magnetic property. The magnetic properties of **Pd-1**, **Pd-2**, and **Pd-3** were investigated using a superconducting quantum interference device (SQUID) magnetometer. All three samples exhibited ferromagnetic behaviors with clear hysteresis loops at 10 K (Figure 3a and b). As the average single domain size of the iron oxide increased, the saturation magnetization ($M_s$) at 10 K increased from 33 emu $g^{-1}$ for **Pd-1** to 60 emu $g^{-1}$ for **Pd-2** and 76 emu $g^{-1}$ for **Pd-3**. The $M_s$ values at 30 K and 100 K were almost identical to those at 10 K for all samples (Figure 3c). At 300 K, the low $M_s$ values of 24 emu $g^{-1}$ for **Pd-1**, 59 emu $g^{-1}$ for **Pd-2**, and 67 emu $g^{-1}$ for **Pd-3** were observed, which were smaller than that of bulk ferrimagnetic $Fe_3O_4$ (84 emu $g^{-1}$).[15] Such size

dependency of $M_s$ can be attributed to the reduced contribution of the surface anisotropy to the magnetic grains as the crystal size

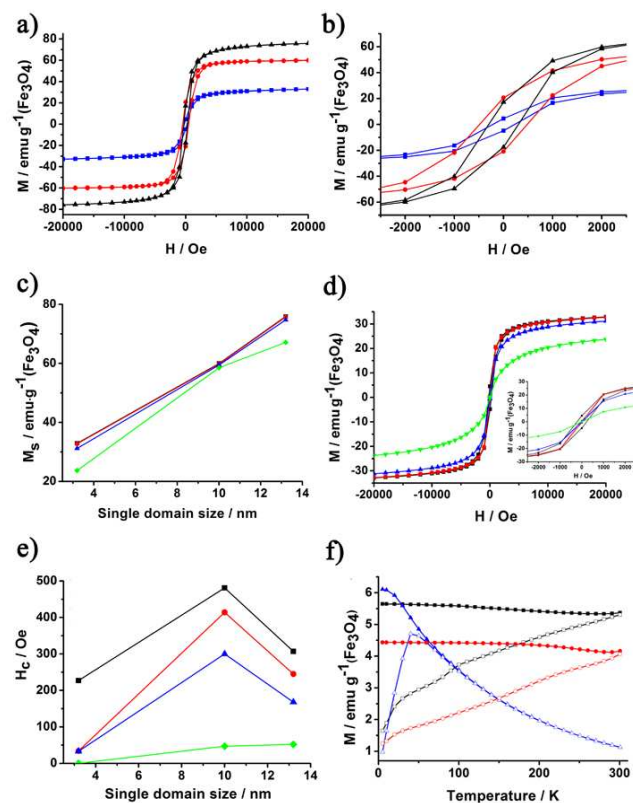

**Fig. 3** M-H curves (a) and magnified M-H curves (b) of **Pd-1** (blue), **Pd-2**
[5] (red), and **Pd-3** (black) measured at 10 K. (c) $M_s$ values versus single-crystal domain size (nm) calculated from XRD data; 10 K (black), 30 K (red), 100 K (blue), and 300 K (green). (d) M-H curves of **Pd-1** measured at different temperatures of 10 K, 30K, 100 K, and 300 K (inset; magnified image). (e) crystal-domain size-dependent $H_c$ values; 10 K
[10] (black), 30 K (red), 100 K (blue), and 300 K (green). (f) zero-field-cooled (ZFC) and field-cooled (FC) magnetic susceptibility of **Pd-1** (blue), **Pd-2** (red), and **Pd-3** (black) (H = 100 Oe).

becomes large.[36] In the temperature range of 10-100 K, **Pd-1**
[15] exhibited a soft ferrimagnetic behavior with a high saturation magnetization and a low coercive force; however, at 300 K, **Pd-1** showed a superparamagnetic property with the zero coercive force, due to the small magnetic grains (Figure 3d).[24] The coercivity ($H_c$) linearly increased from 0 Oe for **Pd-1** to 47 Oe for
[20] **Pd-2** and 52 Oe for **Pd-3** at 300 K, estimated by a horizontal intercept of each hysteresis loop. However, at the temperatures below 100 K, the $H_c$ values approached the maximum for **Pd-2** with the single domain size of 10 nm, which were deviated from the incremental trend. The values of 481, 414, and 300 Oe for
[25] **Pd-2** are significantly larger than 227, 34, and 33 Oe for **Pd-1** and 307, 245, and 168 Oe for **Pd-3** at 10, 30, and 100 K, respectively (Figure 3e). Such anisotropy of the $H_c$ values is in good agreement with previous results.[37] In general, the magnetic dipole-dipole interaction between particles can highly affect the
[30] low-temperature dynamics in a concentrated nanoparticulate system,[38] and lead to the strong magnetic moment anisotropy at

low temperatures.[39,40]

Figure 3f shows the temperature dependent magnetization at 100 Oe. On cooling, the zero-field-cooled (ZFC) and field-cooled
[35] (FC) magnetization curves of **Pd-1** split below 80 K, and the blocking temperature ($T_B$) was 40 K, implying a transition of ferromagnetic to superparamagnetic.[41] Such magnetization behavior of **Pd-1** is similar to that of the 6 nm spherical $Fe_3O_4$ NPs.[36] **Pd-2** and **Pd-3** still exhibit strong hysteretic behaviors at
[40] room temperature, and $T_B$ is higher than 300 K.[42]

### 3.5. Structural anisotropy and catalytic properties

The structural asymmetry of the $Pd-Fe_3O_4$ NPs provided distinct exposure of the active Pd surface outward, which could affect the
[45] diffusion of the reactants and products, and eventually determine the catalytic activity of organic reactions. On this basis, as model catalysts with magnetic recyclability, two extremes of **Pd-1** and **Pd-3** were selected and investigated for a Suzuki cross-coupling reaction between phenylboronic acid and iodobenzene. The
[50] reactions were conducted with 3.0 equiv of $K_2CO_3$ in a solvent mixture of tetrahydrofuran (THF) and water (8:3) at 373 K and the product was analyzed using $^1H$ NMR (Table 1).[20] In entries 1 and 3, the reactions with **Pd-1** and **Pd-3** achieved high product yields of 94 % and 100 %, respectively, with the catalyst loading
[55] of 1.5 mol% Pd for 36 h, indicating that the Pd loading and the reaction time were sufficient for the high yield reaction. The catalysts were readily separated from the reaction mixture with a magnet and it was possible to recycle them twice without loss of product yield due to the high stability of the $Fe_3O_4$ shells under
[60] the basic conditions. Under 0.5 mol% Pd loading for 12 h, **Pd-1** produced biphenyl at a 34% yield, but **Pd-3** still reached a quantitative yield, as shown in entries 2 and 4. The morphologies of **Pd-1** and **Pd-3** were examined after second recycling reaction and no significant change was observed (Figure 4). The low
[65] activity of **Pd-1** was caused by the diffusion barrier of the $Fe_3O_4$ shells for the reactants. The Pd cores were located at the center of mass and were completely surrounded by the shells, although the entire surface of the cores was exposed to the solvent. The reactants approached the catalyst surface only through the grain
[70] boundaries or the defects of the shells, leading to slow diffusion rates. On the other hand, the surface of the Pd cores in **Pd-3** was

**Table 1** Catalytic activity and recyclability of **Pd-1** and **Pd-3** in Suzuki coupling reactions of iodobenzene with phenylboronic acid.



| Entry | Cat. | Pd [mol%] | Time [h] | Conversion [%] [a] | | |
|---|---|---|---|---|---|---|
| | | | | Initial cycle | 1st recycle | 2nd recycle |
| 1 | **Pd-1** | 1.5 | 36 | 94 | 92 | 91 |
| 2 | | 0.5 | 12 | 34 | | |
| 3 | **Pd-3** | 1.5 | 36 | 100 | > 99 | > 99 |
| 4 | | 0.5 | 12 | 100 | | |

[a] The solvents were a mixture of THF and water (8:3), and $K_2CO_3$ (3.0 equiv) was used as a base. All conversion yields were determined by $^1H$
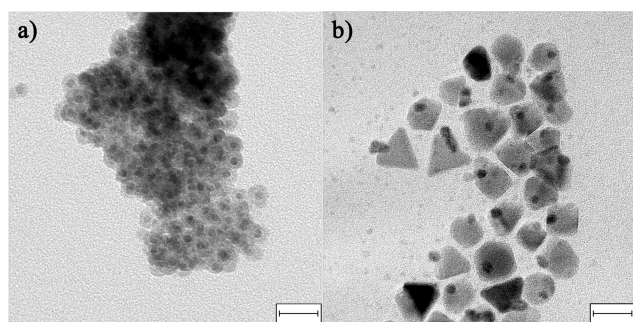[80] NMR.

**Fig. 4** TEM images of recovered a) **Pd-1** and b) **Pd-3** after the second recycling reaction. The scale bars represent 20 nm.

directly exposed to the reaction media without hindrance, and
exhibited high conversion yields.[43]

### 3.6. Synthesis and characterization of Au-Fe₃O₄ hybrid nanoparticles

To extend our strategy of adjusting the structural symmetry and crystallinity, a Au-Fe₃O₄ hybrid system were chosen as another
example, because of its multifunctional properties including optically active Au and magnetically active Fe₃O₄.[11] Although the reaction conditions were different, symmetry alteration in the Au-Fe₃O₄ nanostructures was observed, which was analogous to the case of the Pd-Fe₃O₄ hybrid system. By increasing the ratio of
OA and OAm in the reaction mixture, concentric Au@Fe₃O₄ yolk-shell (**Au-1**, Figure 5a, b, and Supporting Information, Figure S4), Au@Fe₃O₄ yolk-shell with slightly off-centered Au cores (**Au-1'**, Figure 5c and d), acentric Au@Fe₃O₄ core-shell (**Au-2**, Figure 5e and f), and Au-Fe₃O₄ dumbbell-like (**Au-3**,
Figure 5g and h) NPs were generated in sequence. For **Au-1**, the average diameter of the hybrid NPs and the average thickness of the Fe₃O₄ shells were estimated to be 14.3±0.5 nm and 3.1±0.3 nm, respectively (Figure 5a). The HRTEM image shows that the average distances of adjacent lattice fringe images are 0.235 and
0.254 nm, corresponding to face-centered cubic Au (111) and magnetite Fe₃O₄ (311), respectively (Figure 5b). From **Au-1** to **Au-3**, a change of structural symmetry was clearly observed with an increasing ratio of OA versus OAm in the reaction mixture. The **Au-3** structure is dumbbell-like, with an average diameter of
the Fe₃O₄ domains of 20 ± 1 nm (Figure 5g). The average distance of the adjacent lattice fringes in the Fe₃O₄ NPs is 0.298 nm, corresponding to the spacing of Fe₃O₄ (220) (Figure 5h). The average single-crystalline domain sizes of Fe₃O₄, estimated from the XRD data, were 4.5, 11.6, and 22.3 nm for **Au-1**, **Au-2**, and
**Au-3**, respectively (Figure 6a). The electron binding energies of the Au $4f_{7/2}$ level were 83.5 eV for freestanding Au NPs and **Au-1**, and 83.7 eV for **Au-2** and **Au-3** (Figure 6b). The average acentric distance and the crystal domain size of the Fe₃O₄ component increased from **Au-1** to **Au-3**, and the average void
gap between the cores and the shells decreased from **Au-1** to **Au3**, similar to the situation that was observed in the Pd-Fe₃O₄ hybrid system (Figure 6c). The UV-Vis spectra of the Au-Fe₃O₄ hybrid NPs display that the surface plasmon resonance peak of Au becomes more broad from **Au-1** to **Au-3** (Supporting
Information, Figure S5), due to the damping by electronic coupling between the Au and Fe₃O₄ domains.[16] The Au NPs with
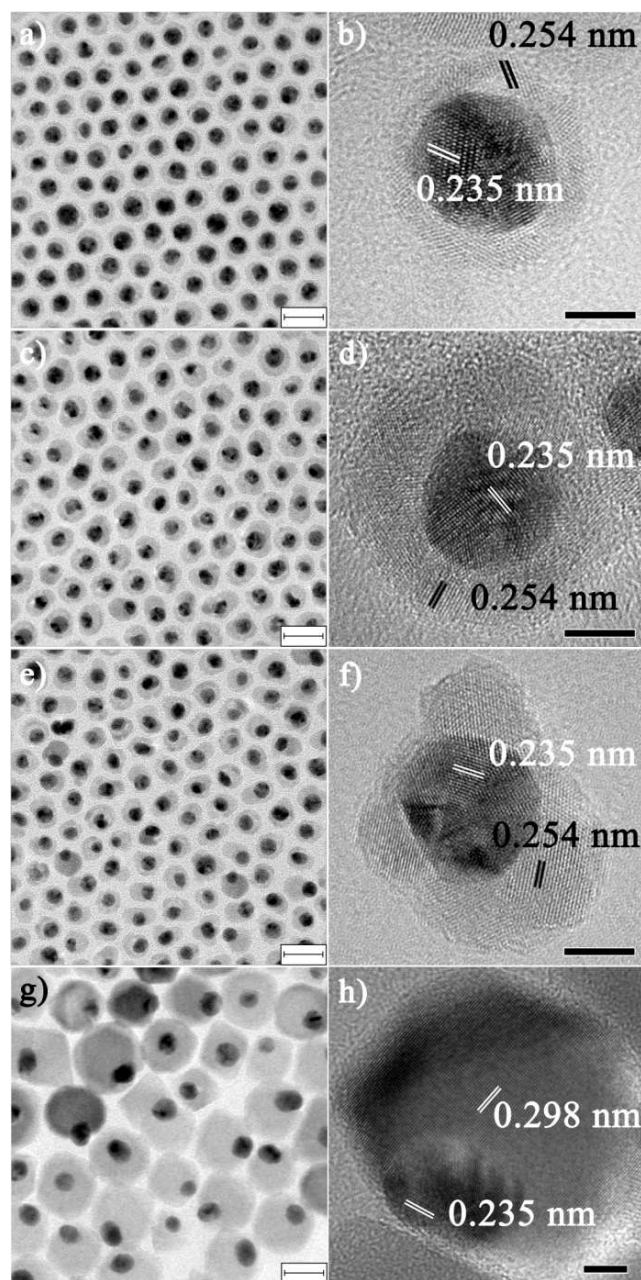


an average

**Fig. 5** TEM and HRTEM images of Au-Fe₃O₄ hybrid NPs synthesized under molar ratios of Fe(CO)₅:OAm:OA; (a, b) **Au-1**, 1 : 40 : 0; (c, d) **Au-1'**, 1 : 36 : 4.2; (e, f) **Au-2**, 1 : 34 : 6.3; and (g, h) **Au-3**, 1 : 32 : 8.4. The scale bars represent (a, c, e, g) 20 nm and (b, d, f, h) 5 nm.

diameter of 10.5 ± 0.5 nm exhibit a strong plasmon absorption at 522 nm, and **Au-1** shows a broad peak at the maximum of 522 nm with a long tail toward a long wavelength region.[16,44] The
plasmon peaks of **Au-2** and **Au-3** are also broad, resulting from the electron transfer to the Fe₃O₄ domains as observed in the XPS data. Further investigation for the optical activity control of Au would enable the Au-Fe₃O₄ system to be a promising multifunctional probe for diagnostic and therapeutic applications.
The Au domains can also be utilized as an optical probe for the

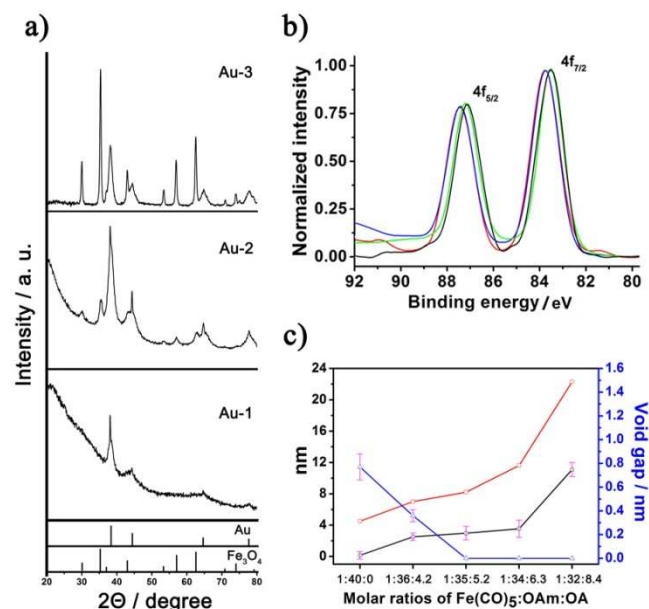monitoring of reactions that occur on the iron oxide surface.



**Fig. 6** (a) XRD data of **Au-1**, **Au-2**, and **Au-3**. (b) Au 4f XPS spectra of freestanding Au NPs (green), **Au-1** (black), **Au-2** (red), and **Au-3** (blue) (Au (111), Φ=5.31 eV; Fe₃O₄ (111), Φ=5.52 eV). (c) The relation of the
5 ratio of capping agents versus average acentric distance (black), crystal domain size (red), and void gap (blue) of each nanostructure in the Au-Fe₃O₄ hybrid system.

## 4. Conclusions

For the metal (Pd or Au)-Fe₃O₄ hybrid system, we demonstrated
10 that the symmetry alteration from concentric yolk-shell to acentric core-shell and dumbbell-like morphologies could be achieved by the precise control of the nucleation and growth kinetics according to the mixture of the two capping agents, OA and OAm. The average crystal domain size of Fe₃O₄ and the void
15 gap between the metal cores and the shells were simultaneously adjusted along with the structural asymmetry. The crystal domain sizes of Fe₃O₄ directly affected the magnetic property, and the structural arrangement of the Pd cores and the Fe₃O₄ shells led to a large difference of conversion yields in the Suzuki coupling
20 reactions. It is expected that this synthetic strategy can be generalized in various metal-metal oxide and metal chalcogenide hybrid systems, in which the reaction steps involve hetero-nucleation and hollow formation by the Kirkendall effect.

## Acknowledgements

## Notes and references

30 *Department of Chemistry, Korea Advanced Institute of Science and Technology, and Center for Nanomaterials and Chemical Reactions, Institute for Basic Science, 291, Daehak-ro, Yuseong-gu, Daejeon, 305-701, Korea. Tel: 82-42-350-2847; E-mail: hsong@kaist.ac.kr*

40 1  D. Wang, Y. Li, *J. Am. Chem. Soc.*, 2010, **132**, 6280.
2   R. Buonsanti, V. Grillo, E. Carlino, C. Giannini, M. L. Curri, C. Innocenti, C. Sangregorio, K. Achterhold, F. G. Parak, A. Agostiano, P. D. Cozzoli, *J. Am. Chem. Soc.*, 2006, **128**, 16953.
3   B. Lim, H. Kobayashi, T. Yu, J. Wang, M. J. Kim, Z.-Y. Li, M.
45   Rycenga, Y. Xia, *J. Am. Chem. Soc.*, 2010, **132**, 2506.
4  Y. Xu, A. Karmakar, D. Wang, M. W. Mahmood, F. Watanabe, Y. Zhang, A. Fejleh, P. Fejleh, Z. Li, G. Kannarpady, S. Ali, A. R. Biris, A. S. Giris, *J. Phys. Chem. C*, 2010, **114**, 5020.
5  W. Shi, H. Zeng, Y. Sahoo, T. Y. Ohulchanskyy, Y. Ding, Z. L.
50   Wang, M. Swihart, P. N. Prasad, *Nano Lett.*, 2006, **6**, 875.
6  Y. Jang, S. Kim, S. W. Jun, B. H. Kim, S. Hwang, I. K. Song, B. M. Kim, T. Hyeon, *Chem. Commun.*, 2011, **47**, 3601.
7   A. J. Amali, R. K. Rana, *Green Chem.*, 2009, **11**, 1781.
8   Z. Wang, B. Shen, Z. Aihua, N. He, *Chem. Eng. J.*, 2005, **113**, 27.
55 9   K. M. Yeo, S. I. Lee, Y. T. Lee, Y. K. Chung, I. S. Lee, *Chem. Lett.*, 2008, **37**, 116.
10  Y. Jang, J. Chung, S. Kim, S. W. Jun, B. H. Kim, D. W. Lee, B. M. Kim, T. Hyeon, *Phys. Chem. Chem. Phys.*, 2011, **13**, 2512.
11   D. Ho, X. Sun, S. Sun, *Acc. Chem. Res.*, 2011, **44**, 875.
60 12   C. Xu, B. Wang, S. Sun, *J. Am. Chem. Soc.*, 2009, **131**, 4216.
13   H. Yin, C. Wang, H. Zhu, S. H. Overbury, S. Sun, S. Dai, *Chem. Commun.*, 2008, 4357.
14   X. Sun, S. Guo, Y. Liu, S. Sun, *Nano Lett.*, 2012, **12**, 4859.
15   E. V. Shevchenko, M. I. Bodnarchuk, M. V. Kovalenko, D. V.
65   Talapin, R. K. Smith, S. Aloni, W. Heiss, A. P. Alivisatos, *Adv. Mater.*, 2008, **20**, 4323.
16  C. Wang, H. Yin, S. Dai, S. Sun, *Chem. Mater.*, 2010, **22**, 3277.
17  C. Wang, Y. Wei, H. Jiang, S. Sun, *Nano Lett.*, 2009, **9**, 4544.
18  C. George, D. Dorfs, G. Bertoni, A. Falqui, A. Genovese, T.
70   Pellegrino, A. Roig, A. Quarta, R. Comparelli, M. L. Curri, R. Cingolani, L. Manna, *J. Am. Chem. Soc,.* 2011, **133**, 2205.
19  M. Kim, J. C. Park, A. Kim, K. H. Park, H. Song, *Langmuir*, 2012, **28**, 6441.
20  J. C. Park, E. Heo, A. Kim, M. Kim, K. H. Park, H. Song, *J. Phys.
75   Chem. C*, 2011, **115**, 15772.
21  S.-W. Kim, J. Park, Y. Jang, Y. Chung, S. Hwang, T. Hyeon, *Nano Lett.*, 2003, **3**, 1289.
22   J. Lee, J. C. Park, J. U. Bang, H. Song, *Chem. Mater.*, 2008, **20**, 5839; J. C. Park, H. Song, *Nano Res.*, 2011, **4**, 33.
80 23   J. C. Park, H. J. Lee, H. S. Jung, M. Kim, H. J. Kim, K. H. Park, H. Song, *ChemCatChem*, 2011, **3**, 755.
24  S. Peng, S. Sun, *Angew. Chem.*, 2007, **119**, 4233.
25  C. Piqure, M. A. Laguna-Marco, A. G. Roca, R. Boada, C. Guglieri, J. Chaboy, *J. Phys. Chem. C*, 2014, **118**, 1332.
85 26  D. R. Lide, *CRC Handbook of Chemistry and Physics*, 86th ed.; CRC Press/Taylor and Francis: Boca Raton, FL, 2005; pp 12-114.
27  C. Wang, H. Daimon, S. Sun, *Nano Lett.*, 2009, **9**, 1493.
28  R. Ouyang, J.-X. Liu, W.-X. Li, *J. Am. Chem. Soc.*, 2013, **135**, 1760.
29  J. Zhang, J. Fang, *J. Am. Chem. Soc.*, 2009, **131**, 18543.
90 30  A. C. S. Samia, J. A. Schlueter, J. S. Jiang, S. D. Bader, C.-J. Qin, X.-M. Lin, *Chem. Mater.*, 2006**, 18***,* 5203.
31  X. Peng, L. Manna, W. Yang, J. Wickham, E. Scher, A. Kadavanich, A. P. Alivisatos, *Nature*, 2000, **404**, 59.
32  X. Peng, J. Wickham, A. P. Alivisatos, *J. Am. Chem. Soc.*, 1998, **120**,
95   5343.
33  Y. Yin, R. M. Rioux, C. K. Erdonmez, S. Hughes, G. A. Somorjai, A. P. Alivisatos, *Science*, 2004, **304**, 711.
34  K. N. Tu, U. Gösele, *Appl. Phys. Lett.*, 2005, **86**, 093111.
35  A. Van der Ven, H.-C. Yu, G. Ceder, K. Thornton, *Prog. Mater. Sci.*,
100   2010, **55**, 61.
36  S.-H. Noh, W. Na, J.-T. Jang, J.-H. Lee, E. J. Lee, S. H. Moon, Y. Lim, J.-S. Shin, J. Cheon, *Nano Lett.*, 2012, **12**, 3716.

37   J. Park, E. Lee, N.-M. Hwang, M. Kang, S. C. Kim, Y. Hwang, J.-G. Park, H.-J. Noh, J.-Y. Kim, J.-H. Park, T. Hyeon, *Angew. Chem.*, 2005, **117**, 2932.

38   M. A. Correa-Duarte, V. Salgueirino, *Nanowires Science and Technology*, In Tech, 2010; pp 83-112.

39   K. J. Klabunde, *Nanoscale Materials in Chemistry*, Wiley-Interscience, New York, 2001; pp 169-221.

40   D. Kim, N. Lee, M. Park, B. H. Kim, K. An, T. Hyeon, *J. Am. Chem. Soc.*, 2009, **131**, 454.

41   G. Gao, X. Liu, R. Shi, K. Zhou, Y. Shi, R. Ma, E. Takayama-Muromachi, G. Qiu, *Crystal Growth & Design*, 2010, **10**, 2888.

42   Y. Xiao, S. Ge, L. Xi, Y. Zuo, X. Zhou, B. Zhang, L. Zhang, C. Li, X. Han, Z. Wen, *Appl. Surf. Sci.*, 2008, **254**, 7459.

43   S. Chen, R. Si, E. Taylor, J. Janzen, J. Chen, *J. Phys. Chem. C*, 2012, **116**, 12969.

44.  H. Yu, M. Chen, P. M. Rice, S. X. Wang, R. L. White, S. Sun, *Nano Lett.*, 2005, **5**, 379.

# Journal of Materials Chemistry C

Dynamic Article Links ▶

**Full Papers**

## Graphical Abstract

The symmetry alteration from concentric yolk-shell to acentric core-shell and dumbbell-like morphologies in metal-$Fe_3O_4$ hybrid system

5 is achieved by the precise control of the nucleation and growth kinetics of Fe on the metal surface. Along with the structural asymmetry,

crystallinity of $Fe_3O_4$ and the Kirkendall void gap are simultaneously adjusted, and they directly affect the magenetic and catalytic

properties.



10

15

Journal of Materials Chemistry C Accepted Manuscript
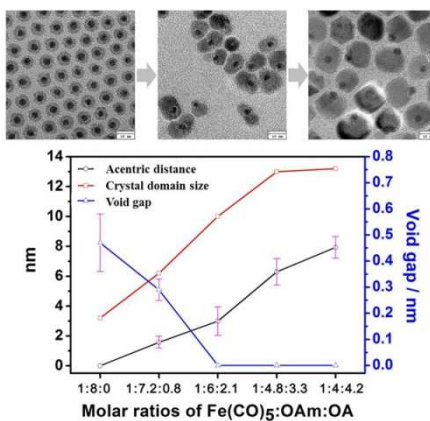
# Supplementary Information

## Precise Adjustment of Structural Anisotropy and Crystallinity on Metal-Fe$_3$O$_4$ Hybrid Nanoparticles and Its Influence on Magnetic and Catalytic Properties
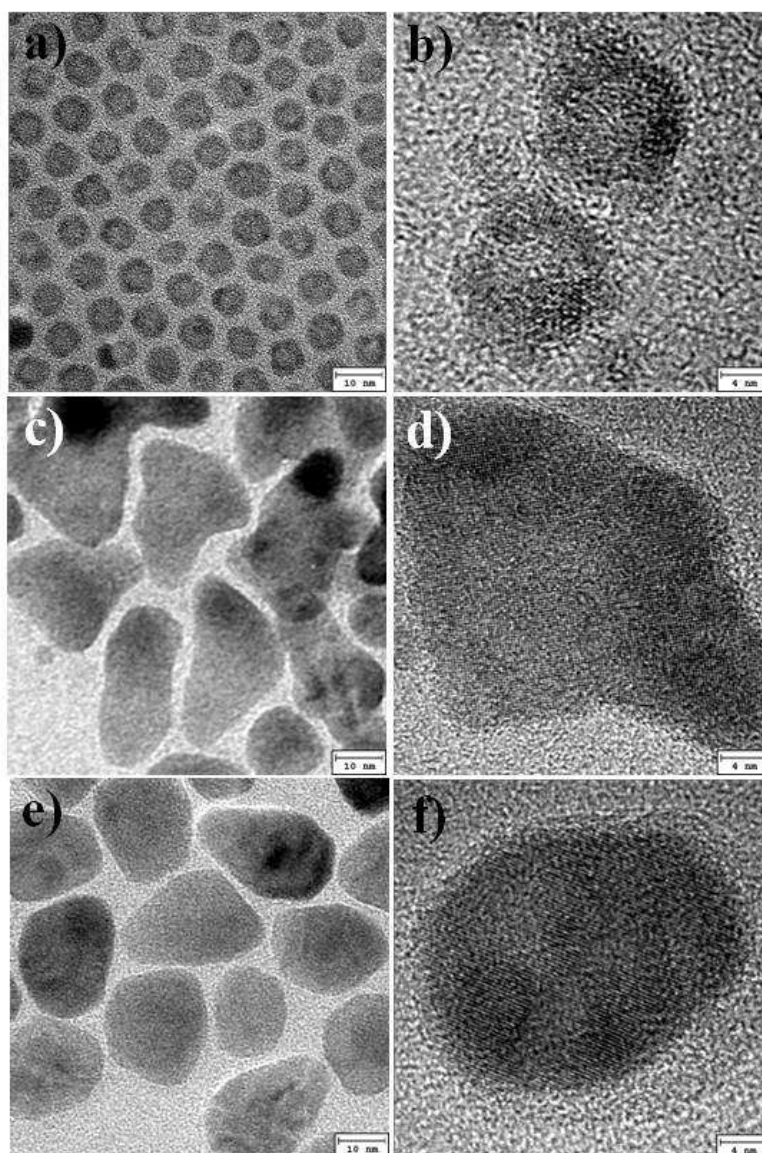
**Mijong Kim and Hyunjoon Song***

**Fig. S1** TEM images of Fe$_3$O$_4$ NPs prepared under the reaction conditions identical to the synthetic process of **Pd-1**, **Pd-2** and **Pd-3** except for the injection of Pd seeds. a, b) **Pd-1**, c, d) **Pd-2** and e, f) **Pd-3** without Pd seed parts. The bars represent a,c,e) 10 nm and b,d,f) 4 nm, respectively.
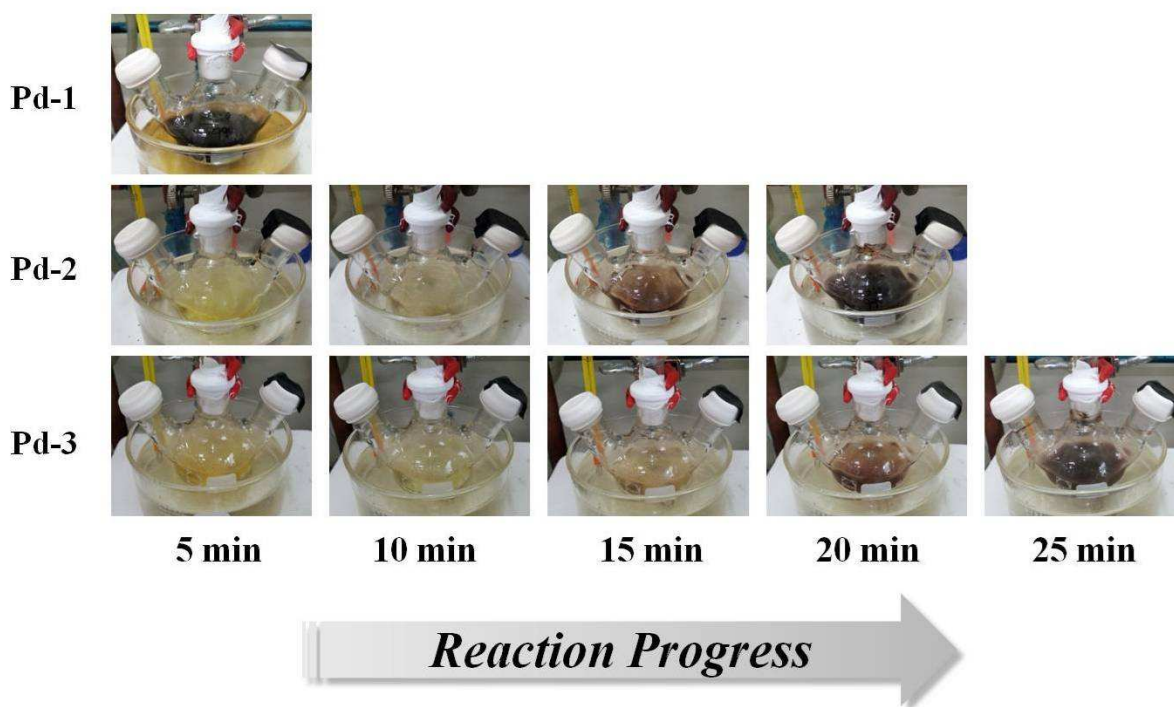
**Fig. S2** Color changes of the reaction mixtures of **Pd-1**, **Pd-2** and **Pd-3** in the absence of metal seeds during the synthetic process (**Pd-1**, Fe(CO)$_5$ : OAm : OA = 1 : 8 : 0, **Pd-2**, 1 : 6 : 2.1, **Pd-3**, 1 : 4 : 4.2).
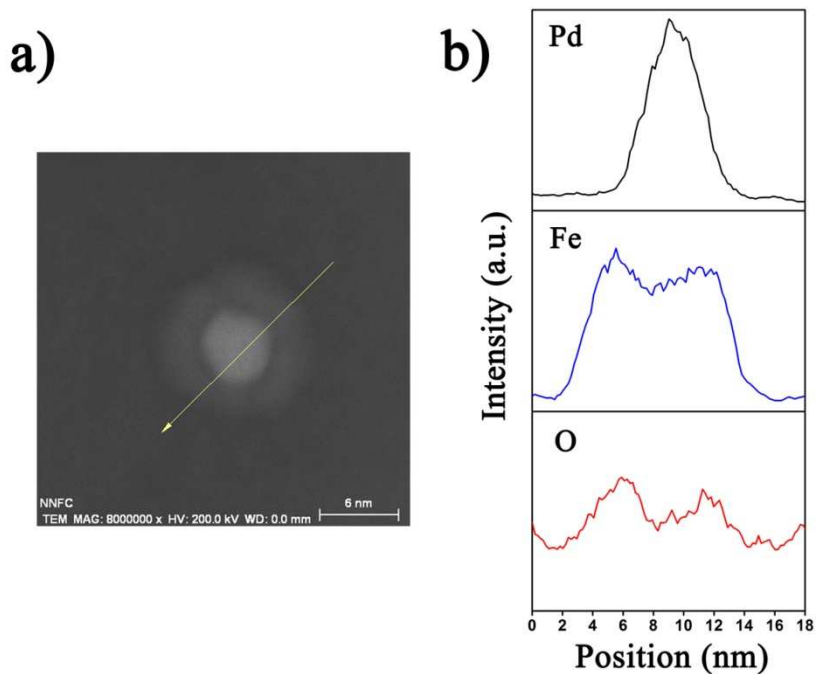
5



10 **Fig. S3** a) High-magnification HAADF-STEM image of a single **Pd-1** and b) spatial elemental distribution obtained from EDX line-scan measurement.
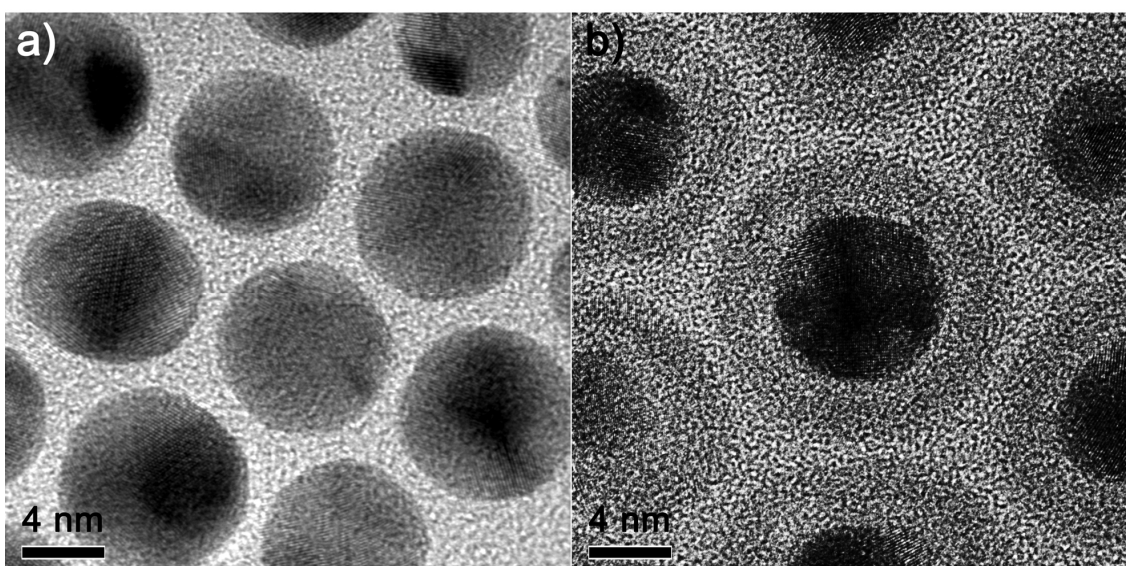
**Fig. S4** TEM images of a) Au NPs and b) **Au-1** (Au@Fe$_3$O$_4$ yolk-shell NPs). The bright area between Au core and Fe$_3$O$_4$ shell is the void area caused by Kirkendall effect.
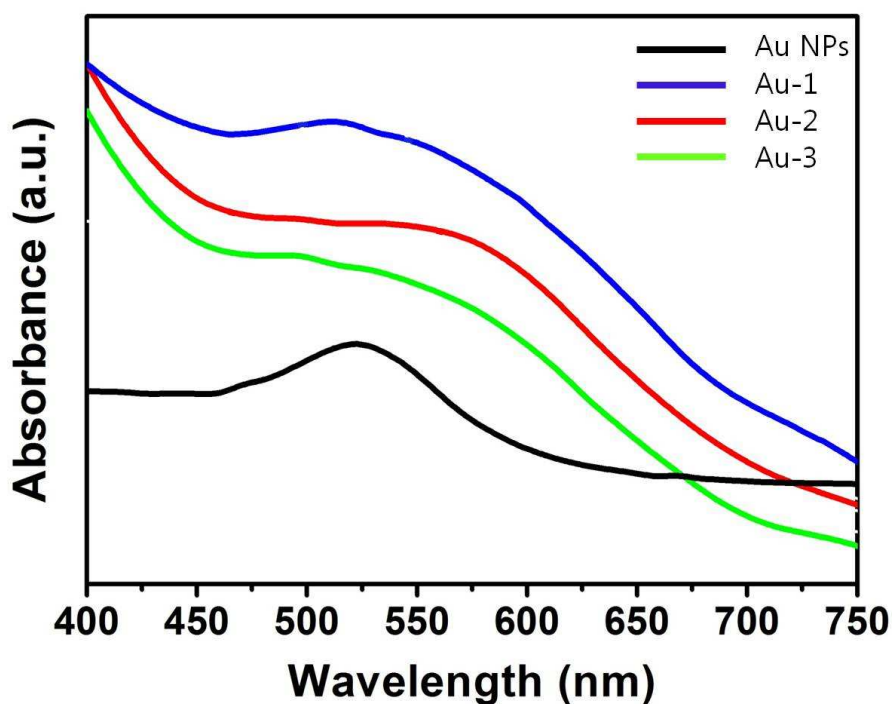


**Fig. S5** UV-Vis spectra of Au NPs, **Au-1**, **Au-2**, and **Au-3**.